

## OPTICAL SPECTROSCOPY AND NARROW-BAND IMAGES OF THE VARIABLE SEYFERT 1 GALAXY NGC 3783<sup>1</sup>

CLAUDIA WINGE,<sup>2</sup> M. G. PASTORIZA<sup>2,3</sup> AND T. STORCHI-BERGMANN<sup>3</sup>

Departamento de Astronomia, Instituto de Física, Universidade Federal do Rio Grande do Sul, Avenida Bento Gonçalves, 9500, CP15051, CEP 91500, Porto Alegre, RS, Brazil

AND

S. LIPARI<sup>3,4</sup>

Space Telescope Science Institute, 3700 San Martin Drive, Baltimore, MD 21218

Received 1991 September 16; accepted 1991 December 30

### ABSTRACT

We present narrow-band images centered on [O III]  $\lambda$ 5007, H $\alpha$ , and adjacent continua of the Seyfert 1 galaxy NGC 3783. The continuum images evidence that the bar emission is mainly due to old stars. The [O III]  $\lambda$ 5007 image shows that the high-excitation gas is very concentrated while the H $\alpha$  emission is more extended and elongated perpendicularly to the direction of the bar.

Ten new optical spectra, obtained between 1987 and 1990, are used to study the variability of the continuum and emission lines in this galaxy. The contribution of the bulge stellar population to the nuclear spectrum is determined for each epoch and subtracted. The remaining optical continuum is then decomposed in two variable components, and after these components have been subtracted, the resultant spectra, constituted by pure line emission, are analyzed. A multiple Gaussian components model is found in order to describe the different emission lines on the various spectra. With the results of this decomposition the structure and physical conditions of the emission-line regions are determined. The variations in the continuum and emission-line fluxes are then analyzed, and the relations between them are pointed out.

*Subject headings:* galaxies: individual (NGC 3783) — galaxies: Seyfert — galaxies: stellar content

### 1. INTRODUCTION

NGC 3783 is a southern Seyfert 1 galaxy with very strong emission lines, and it was the subject of several investigations: optical spectrophotometry has been carried out by Martin (1974), Osmer, Smith, & Weedman (1974), Cooke et al. (1976), and Penston et al. (1977); mid-infrared photometry was made by Glass et al. (1982), and *IUE* spectra were analyzed by Barr, Willis, & Wilson (1983) and Wamsteker & Barr (1985). It is an X-ray source (Cooke et al. 1976), and its X-ray spectrum is known to be variable (Branduardi-Raymont et al. 1985). Analysis of the emission-line profiles has been performed by Pelat, Alloin, & Fosbury (1981), and by Evans (1988). Variability of the nuclear continuum light in the optical and infrared has been reported by Penfold (1979), Glass (1979), de Ruiter & Lub (1986), and Hamuy & Maza (1987). Strong variations of the broad component of the Balmer and He lines were observed, not only in flux (Atwood, Baldwin, & Carswell 1982; Ward & Morris 1984; Morris & Ward 1988; Stirpe, de Bruyn, & van Groningen 1988; Evans 1989), but also in shape (Menzies & Feast 1983).

In this paper we present narrow-band imagery (H $\alpha$  and [O III]  $\lambda$ 5007) and 10 new optical spectra of this galaxy, analyzing the gas morphology and extension, the bulge stellar population contribution to the nuclear spectra, and the continuum

and emission-line shapes and variability. A value of  $H_0 = 50 \text{ km s}^{-1} \text{ Mpc}^{-1}$  is assumed throughout this work.

### 2. THE OBSERVATIONS

The data analyzed here consist of 10 optical spectra obtained at three observatories: the Cerro Tololo Interamerican Observatory (CTIO, Chile), the Laboratório Nacional de Astrofísica (LNA, Brazil), and the Complejo Astronómico del Leoncito (CASLEO, Argentina), including different spectral ranges between 3700 and 8000 Å with resolutions from 5 to 14 Å, and four CCD images centered on (redshifted) H $\alpha$   $\lambda$ 6563 and [O III]  $\lambda$ 5007 lines, and adjacent continua.

#### 2.1. The CCD Images

The images were obtained with the CTIO 91 cm telescope plus CCD Ti2 on 1990 March 11–13. The integration times and filter specifications are listed in Table 1. The image scale is  $0''.494 \text{ pixel}^{-1}$ . The reduction of the images follows standard procedures (IRAF packages). The flux calibration was made using images of standard stars from Stone & Baldwin (1983). Once flux calibrated each continuum image was subtracted from its respective line + continuum one, to produce the pure H $\alpha$  and pure [O III] emission images (hereafter  $p\text{H}\alpha$  and  $p[\text{O III}]$ , respectively).

#### 2.2. The Optical Spectra

NGC 3783 was observed in 10 epochs during the period 1987 March to 1990 June. The log of observations is presented in Table 2. The columns list by order the following:

The run number (as each observation will be referred to hereafter);

<sup>1</sup> Based on observations obtained at the CTIO (Chile), at the Laboratório Nacional de Astrofísica (Brazil), and at the Complejo Astronómico del Leoncito (Argentina).

<sup>2</sup> CNPq Fellowship.

<sup>3</sup> Visiting Astronomer at the Cerro Tololo Interamerican Observatory of the National Optical Observatories, operated by AURA under contract with the National Science Foundation.

<sup>4</sup> Visiting Astronomer at CASLEO, Argentina.

TABLE 1  
OBSERVING LOG: CCD IMAGES

Image (1)	Date (2)	$T_{\text{exp}}$ (s) (3)	$\lambda_0$ (Å) (4)	FWHM (Å) (5)	Peak (6)
H $\alpha$ .....	1990 Mar 11	900	6606	75	242
H $\alpha$ Continuum .....	1990 Mar 11	1200	6477	75	40
[O III] .....	1990 Mar 13	900	5057	15	42
[O III] Continuum ....	1990 Mar 13	900	4740	190	22

NOTES.—Col. (3): Total integration time, in seconds; col. (4): filter central wavelengths; col. (5): filter widths; col. (6): innermost isophotes values, in units of  $10^{-15}$  ergs  $\text{cm}^{-2}$   $\text{s}^{-1}$ .

The observation date, with the correspondent JD conversion;

The telescope/detector used;

The slit dimensions (the table gives the slit width [N-S]  $\times$  length [E-W] dimensions. When only one figure is given, it corresponds to the slit width, and the spectra are integrated over the total extension of the galaxy);

The wavelength coverage/final resolution of each spectrum.

All the spectra were reduced following standard spectrophotometric techniques and flux calibrated using standard stars from the lists of Oke & Gunn (1983), Stone & Baldwin (1983), and Taylor (1984).

The nuclear spectra were corrected from reddening using the curves of Seaton (1979), and adopting a color excess  $E(B-V) = 0.09$ , due to the Galactic extinction only.

The redshift of each spectrum was obtained by averaging the values separately calculated from the observed main forbidden emission lines and narrow components of H $\alpha$  and H $\beta$ , and the individual data were corrected by this mean. The value obtained for the systemic velocity of NGC 3783 from the whole set of observations is  $v = 2930$  km  $\text{s}^{-1}$ , which gives a distance of 58.6 Mpc for the galaxy and a linear scale of 285 pc arcsec $^{-1}$ .

During the 1987 CTIO run, we have also obtained a spectrum of a region 8" north of the nucleus. Another off-nuclear spectrum was extracted from the 2D-FRUTTI original frame of the 1988 observation, being composed by the sum of two 25 arcsec $^2$  regions centered 5" east and west of the nucleus. These spectra were reduced the same way as the nuclear ones, but were also corrected by an additional color excess (internal to the galaxy) of  $E(B-V) = 0.14$  (Forte et al. 1987). They have

TABLE 2  
OBSERVING LOG: OPTICAL SPECTRA

Run (1)	Date (2)	JD (2,441,000+) (3)	Equipment (4)	Slit (5)	Interval/Resolution (6)
1 .....	1987 Mar 2	5857	1.0/2DF	5 $\times$ 8	3700–7100/5
2 .....	1988 May 10	6292	1.0/2DF	5 $\times$ 5	3600–6900/5
3 .....	1988 Jun 8	6321	1.6/OMA	6	4600–8900/12
4 .....	1989 May 8	6655	1.6/OMA	3	4450–8100/14
5 .....	1989 May 10	6657	2.15/Rt	3	4400–6900/7
6 .....	1989 Jun 28	6706	2.15/Rt	3	4650–7100/7
7 .....	1989 Jul 15	6723	1.6/OMA	3	4500–7100/14
8 .....	1990 Mar 3	6954	1.0/2DF	2 $\times$ 8	3600–7050/5
9 .....	1990 Mar 27	6978	2.15/Rt	3	4250–7100/7
10 .....	1990 Jun 25	7068	2.15/Rt	3	4650–7600/7

NOTES.—Column (4): 1.0/2DF = CTIO 1.0 m + 2D FRUTTI; 1.6/OMA = LNA 1.6 m + OMIII; 2.15/Rt = CASLEO 2.15 m + Reticon; col. (5): slit dimensions in arcseconds; col. (6): interval and resolution in Å.

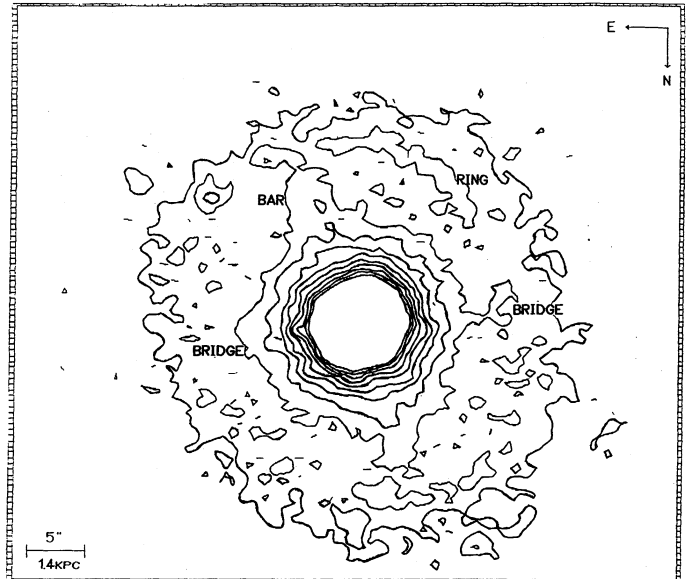


FIG. 1.—The H $\alpha$  + continuum image, with the structures discussed in the text. Contours from  $F_{\lambda} = 0.2$ –2.0.

been already analyzed by Winge, Storchi-Bergmann, & Pastoriza (1990), and we will briefly summarize these previous results in § 4.2.1, where we discuss the stellar population of NGC 3783 and its contribution to the nuclear light.

The spectra of runs 4 and 5 are constituted by the average of three and two observations, respectively, obtained on consecutive nights on 1989 May 9–11 and June 27–28. These spectra have been analyzed to search for variability on time series scales of 1 or 2 days, but we found no evidence of such short-time variations.

### 3. IMAGES AND MORPHOLOGY OF THE GAS EMISSION

Figures 1–3 show the CCD images, the lowest isophotal level of each image being placed  $1 \sigma$  above the residual background left by the sky subtraction. The contours on these figures are given in flux units of  $10^{-15}$  ergs  $\text{cm}^{-2}$   $\text{s}^{-1}$ , and as we are mainly interested in the disk and near-nucleus features, only the isophotal contours up to the  $F_{\lambda} = 2.2 \times 10^{-15}$  ergs  $\text{cm}^{-2}$   $\text{s}^{-1}$  level are shown. The values of the peak isophotes are given in Table 1.

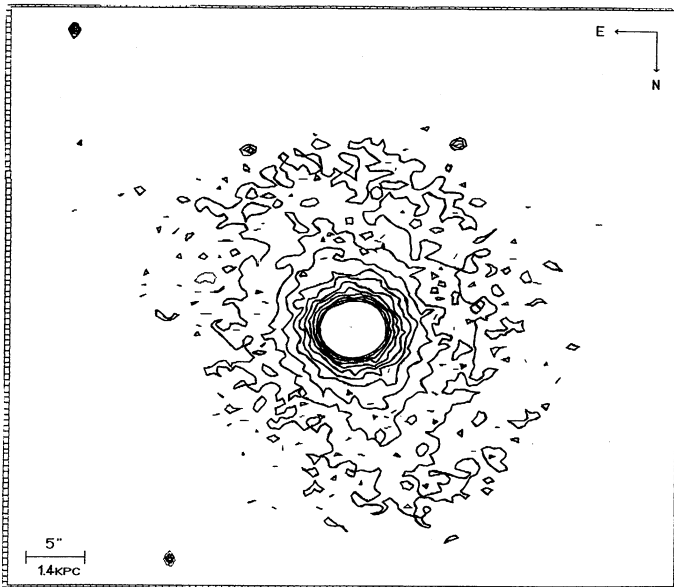


FIG. 2a

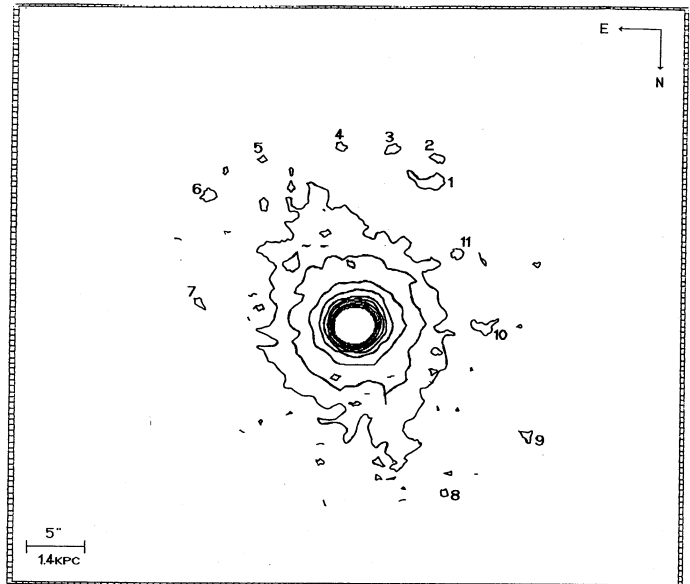


FIG. 2b

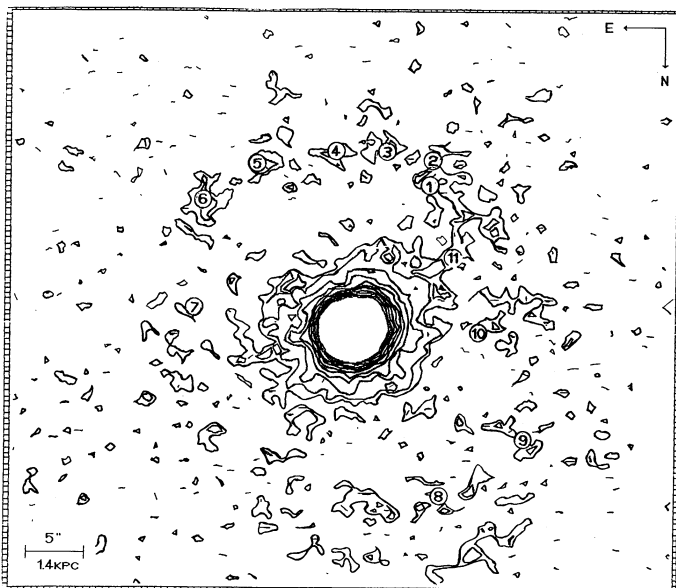


FIG. 2c

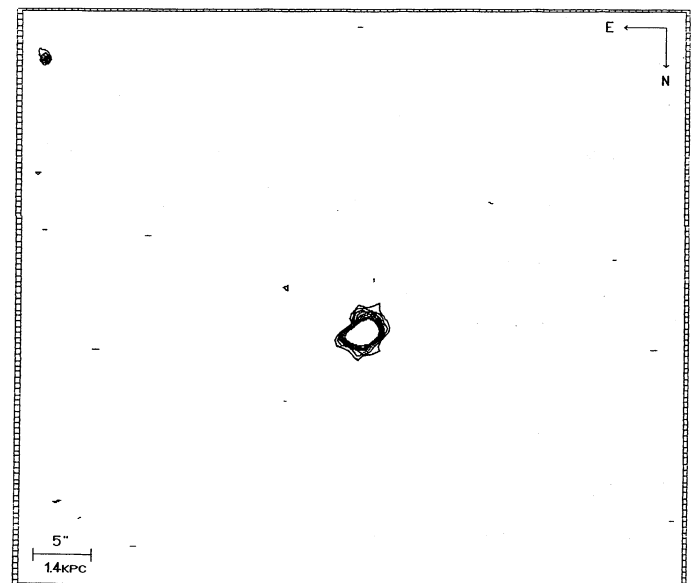


FIG. 2d

FIG. 2.—(a) Red continuum (contours at  $F_{\lambda} = 0.2, 0.4$ , etc.); (b) blue continuum ( $F_{\lambda} = 0.1, 0.2, 0.4$ , etc.); (c) pure  $H\alpha$  ( $F_{\lambda} = 0.1, 0.2, 0.4$ , etc.); and (d) pure  $[O\text{ III}]$  ( $F_{\lambda} = 0.2, 0.4$ , etc.) images.

The main structures of interest are indicated on Figure 1, over the  $H\alpha$  + continuum image. Clearly visible are the bar (at P.A. =  $163^{\circ}5$ ; Forte et al. 1987, hereafter F87), parts of the inner ring, and two structures oriented perpendicularly to the bar, already detected by F87 and that they called “the bridges.” The western bridge is more evident, joining the central isophotes and the ring.

As our blue (4740 Å) continuum image includes the contribution from the  $He\text{ II } \lambda 4686$  line in the filter bandpass, we have estimated it applying the filter response curve over the run 8 spectrum (that is, approximately contemporaneous with the images) and obtained that it is of about 7% for the inner

$2'' \times 8''$  region. So we can expect a small underestimation of the  $p[O\text{ III}]$  flux, but the shape of the image contours will remain essentially unchanged, even if the  $He\text{ II } \lambda 4686$  and  $[O\text{ III}]$  emission gas distributions are different.

In Figure 2, corresponding to the continuum and pure-line images, we can observe that the central contours (up to a  $5''$  radius) are nearly circular on all the images, except  $p[O\text{ III}]$ , where the isophotes are asymmetric, being elongated in the direction of the bridges, as can be more clearly seen in the enlargement of the central  $10'' \times 10''$  (Fig. 3). The regular contours for a field star (shown as an insert on Fig. 3) confirm the reality of this asymmetry. The external contours are progres-

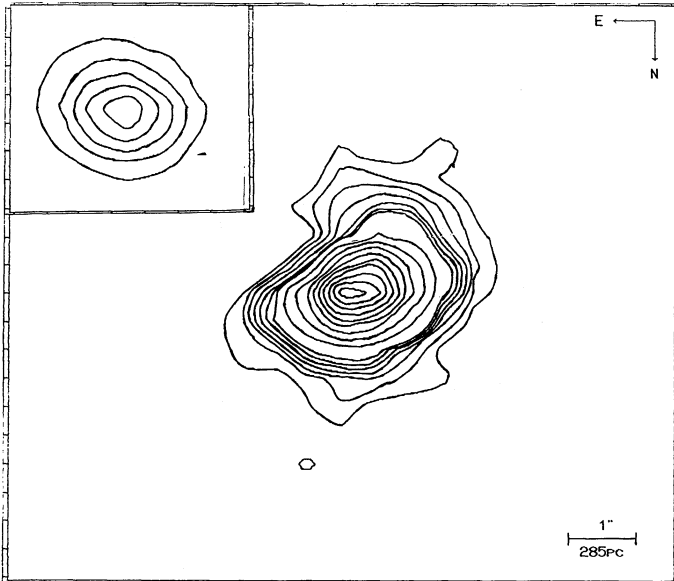


FIG. 3.—Enlargement of the inner  $10'' \times 10''$  of Fig. 2d

sively more elongated, and oriented following the direction of the bar on the continuum images, but perpendicularly to it on the  $pH\alpha$  one.

A very interesting and evident characteristic (see Figs. 1 and 2c,  $H\alpha$  + continuum and  $pH\alpha$  images, respectively) is the absence of  $H\alpha$  emission along the bar, while the emission along the bridges (mainly at P.A.  $\approx 230^\circ$ , the western bridge) is easily seen. It can also be noted in the inner ring and part of the northern spiral arm.

From the superposition of the  $pH\alpha$  and the blue (4740 Å) continuum images, we notice that the knots that appear on the continuum image (numbered 1–11) are coincident with the brightest regions of  $H\alpha$  emission on the inner ring.

Considering the features described above, we can conclude that the high-excitation gas (responsible for the [O III] emission) is highly concentrated and slightly asymmetrically distributed, extending up to 400 pc from the nucleus on our image. The  $H\alpha$  emission is also asymmetric, being elongated perpendicularly to the bar direction, and extends to more than 2 kpc. The presence of the bridges in the direction of the elongation points toward the existence of a liaison between the gas of the nuclear region and that of the ring. It is also important to point out that the absence of gas emission along the bar, that is observed only on the continuum images. The fact that the bar is brighter in the red (6477 Å) than in the blue (4740 Å) continuum indicates that old stars are responsible for the majority of the flux from this structure. Since the blue continuum represents the emission from the younger stellar population, and recalling that the outer “knots” in Figure 2b are coincident with the brightest parts of pure  $H\alpha$  emission of the ring, we can conclude that the gas in the inner ring is ionized by hot stars.

Finally, since the emission that characterizes the bridges is much stronger on the  $pH\alpha$  image than on the  $H\alpha$  continuum one, we can attribute such emission to gas ionized by a power-law spectra (Winge et al. 1990), instead of to electron scattering of the central source continuum, as suggested by F87.

## 4. SPECTRA

### 4.1. Normalization

It became a usual practice in optical variability studies to use the strongest forbidden line fluxes (usually [O III]  $\lambda 4959$  and/or  $\lambda 5007$ ) to normalize different spectra to the same flux scale.

This kind of “internal calibration” could reach an accuracy on the line fluxes better than 5% (Stirpe et al. 1988; Peterson et al. 1991), but requires the whole narrow-line region (NLR) of the observed AGN to be contained inside the spectrograph slit during all the integration time of each observation.

As discussed in § 3, the [O III]  $\lambda 5007$  emission in NGC 3783 is very concentrated. From a north-south profile extracted from our  $p$ [O III] image, we have found that about 99% of the [O III]  $\lambda 5007$  emission in this image comes from the central  $5'' \times 5''$  ( $1.4 \times 1.4$  kpc) region. The smallest slit width used in our set of spectra ( $2'' \times 8''$ ) still contains more than 87% of this line emission. A similar analysis performed on a profile extracted from the  $pH\alpha$  image yields that a  $5'' \times 5''$  slit corresponds to 95% of the  $H\alpha$  emission. Assuming that the [O III] line flux is constant over the entire set of observations (Peterson 1988), we have measured the [O III]  $\lambda 4959$  flux in all the spectra and normalized the data to the flux of this line in the 1988 May 10 (run 2) spectrum,  $F_{[\text{O III}] \lambda 4959} = 105 \times 10^{-15}$  ergs  $\text{cm}^{-2} \text{s}^{-1}$ .

Since the [O III]  $\lambda 4959$  line is located just over the red wing of  $H\beta$ , the reference spectrum is selected as the one where this contamination was smaller, and we have used the [O III]  $\lambda 4959$  rather than the stronger [O III]  $\lambda 5007$  due to the fact that the latter is saturated on the run 3 (and possibly on the run 7) spectrum.

As already pointed out in § 1, NGC 3783 is a strongly variable Seyfert 1 galaxy. This behavior can also be seen in our data when comparing the normalized spectra: Figure 4 shows the run 2 and 8 spectra (that can be interpreted as states of “low” and “high” activity, respectively), as well as their difference, to illustrate the variations of the permitted lines and continuum during the period of our observations.

### 4.2. The Observed Optical Continuum

To represent the continuum of NGC 3783 in our optical spectra, we assumed that it can be described as a sum of, at least, two components: the bulge stellar population of the host galaxy and a power-law continuum ( $F_\nu = \nu^{-\alpha}$ , with  $\alpha$  positive and variable) (Begelman 1988; Stein & O’Dell 1985).

#### 4.2.1. The Stellar Population Contribution at Low Activity

Using the off-nuclear spectra cited in § 2.2, we have determined the age and metallicity of the bulge stellar population of NGC 3783. This analysis has been described elsewhere (Winge et al. 1990), and here we will only summarize the relevant results: we have found that the stellar population of the galaxy bulge can be represented by the S4 template of Bica (1988) and is mainly old (82% of the flux at 5870 Å is due to a population older than 5 Gyr) with some contribution from intermediate-age and moderately young stars and of solar metallicity. We have also found that the emission-line ratios measured on the off-nuclear spectra indicate that the gas as far as 2 kpc from the nucleus is still photoionized by a power-law continuum.

Once we have obtained representation for the bulge stellar population the next step is to quantify its contribution to the nuclear spectrum. In previous works (Evans 1988; Ward et al.

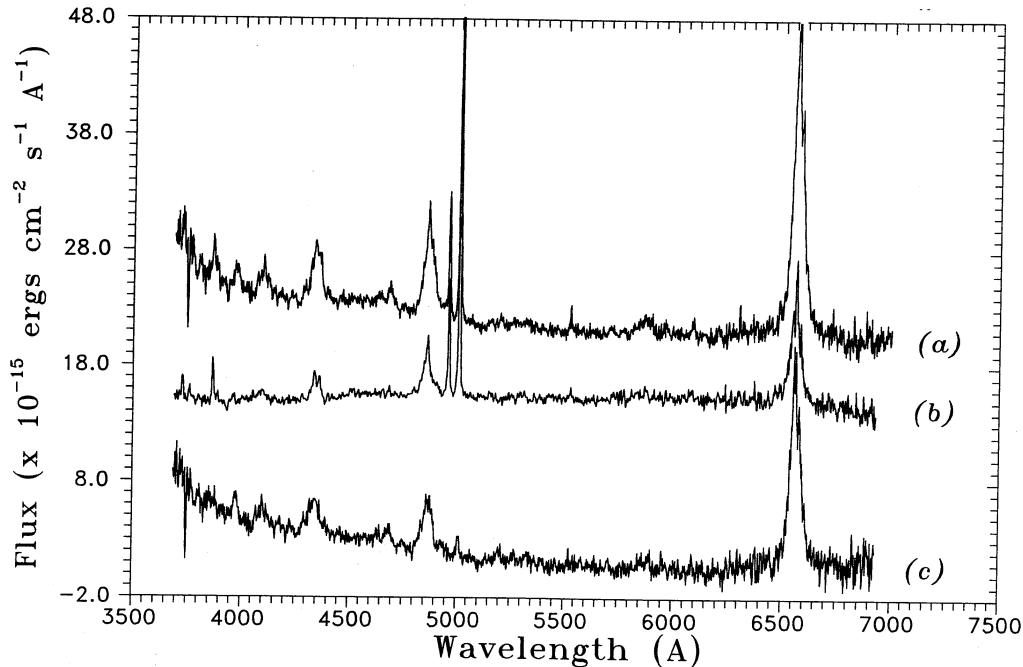


FIG. 4.—(a) High (run 8) and (b) low (run 2) states of NGC 3783 and (c) difference between them. Notice the strong variation in the continuum shape as well as intensity, and in the line fluxes.

1987) this contribution has been considered as negligible, due to the narrow slits and strong nonthermal (power-law) emission. However, as can be seen in Figure 5a, the run 2 spectrum is contaminated by the galaxy stellar population, presenting a flat or even positive slope, as well as the Ca II K and H  $\lambda\lambda 3933$ , 3968 CH G band, Mg I + MgH  $\lambda 5175$  and Na I  $\lambda 5890$  absorption lines.

To have a first approach to the level of activity of the source at this epoch, we have collected the ratio  $I(\text{H}\beta)/I([\text{O III}] \lambda 4959)$  from the available literature, and the result including our own data is shown in Figure 6 as a function of time. It can be noted that the run 2 spectrum corresponds to a state of low activity of

the source, also observed in 1972, 1977, and 1981, and is characterized by a mean value of  $I(\text{H}\beta)/I([\text{O III}] \lambda 4959) = 2.1 \pm 0.4$ .

Assuming that the run 2 spectrum represents the lowest level of activity reached by NGC 3783, the bulge stellar population contamination derived from this spectrum will represent the greatest contribution of the host galaxy to the nuclear light in this object, for the central  $5'' \times 5''$ .

To determine this contribution, the S4 template was normalized in order to represent 5% of the nuclear light at 5600 Å and repeatedly subtracted from the run 2 spectrum until the Mg I + MgH line was reduced to the noise level.

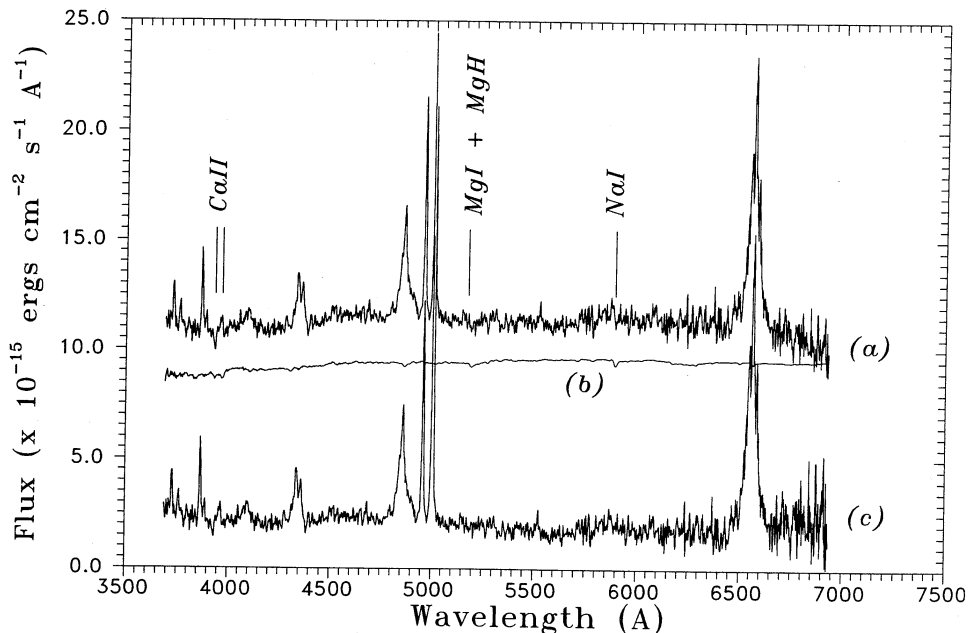


FIG. 5.—State of low-activity (run 2) spectrum before (a) and after (c) the subtraction of the bulge stellar population template (b) as described in the text. A constant has been added to spectra (a) and (b) for clarity.

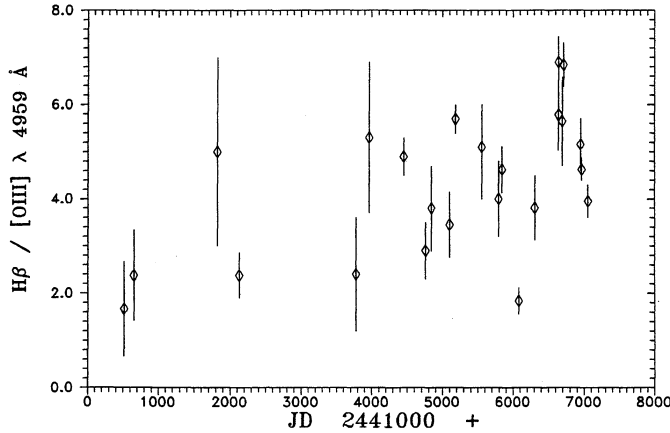


FIG. 6.— $H\beta/[O\text{ III}] \lambda 4959$  light curve for NGC 3783 from 1974 to 1990

Figure 5c shows the nuclear spectrum after the subtraction of a stellar contribution correspondent to  $50\% \pm 5\%$  of the nuclear light at  $5600 \text{ \AA}$  (shown in Fig. 5b). Notice the changes in the continuum shape and the emission lines (especially  $H\epsilon \lambda 3970$ ).

We have then, obtained that the S4 template normalized to a flux of  $F_\lambda = 1.566 \times 10^{-16} \text{ ergs cm}^{-2} \text{ s}^{-1} \text{ \AA}^{-1}$  at  $5600 \text{ \AA}$  represents the total amount of stellar population contribution to the nuclear spectrum of NGC 3783 for a integration area corresponding to the central  $5 \times 5 \text{ arcsec}^2$ .

#### 4.2.2. Stellar Population Contribution for Different Slits

To derive an appropriate correction for the different areas encompassed by the slits used, we have considered that the flux of the continuum can be written, for any epoch,

$$F_{\text{continuum}} = F_{\text{bulge}} + F_{\text{AGN}},$$

where  $F_{\text{bulge}}$  is the bulge stellar population contribution, dependent of the slit used, and of the bulge's light distribution, but constant in time.

$F_{\text{AGN}}$  is the central source plus emission-line region contribution, variable in time but independent of the slit used.

The stellar population contribution to the total flux of each spectra was calculated from the spatial profile for  $5600 \text{ \AA}$ , extracted from the 2D-FRUTTI original frame of run 2 (1988 May 10). This curve, presented in Figure 7, represents the

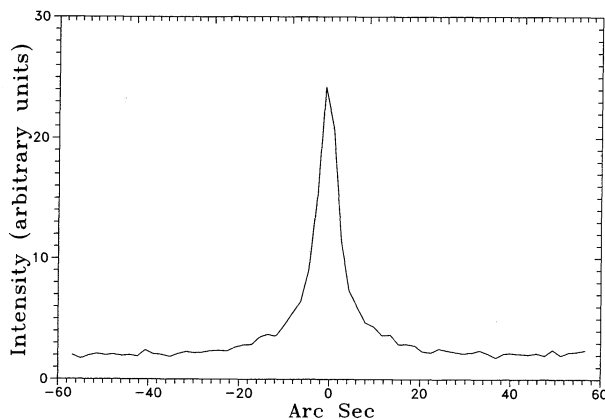


FIG. 7.—Spatial profile at  $5600 \text{ \AA}$ , normalized as described in the text

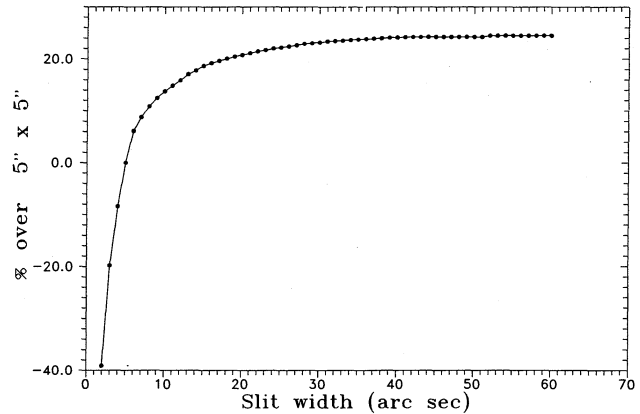


FIG. 8.—Dependence of the stellar population contribution with the dimensions of the slit, referred over the inner  $5'' \times 5''$  contribution.

galaxy light distribution at  $\lambda 5600$ , integrated over the  $5''$  of the slit width.

The next step was to integrate the central  $5''$  on the profile (which will correspond to the central  $25 \text{ arcsec}^2$  emission) and normalize the resulting value to 100. With this procedure, we have determined that the contribution due to the nonthermal and stellar population components each amount to 50. Then, integrating the profile in successively greater areas (slits of  $5'' \times 6''$ ,  $5'' \times 7''$ , etc.), and since the nonthermal contribution remains 50, we can construct the curve of Figure 8, which will be used to derive the stellar contribution for a given slit area, assuming that the stellar population is homogeneous (i.e., it can be represented on every point of the bulge by the S4 template). From this figure, we obtain the appropriate multiplicative factors that scale the stellar population contribution of the inner  $25 \text{ arcsec}^2$  to each one of the different slit areas used. Notice that for those slits which include the total length of the galaxy, the saturation value of the curve, 24.5%, is used.

The scaling factors for the several spectra are presented in the second column of Table 3, and the third column gives the percentual stellar population contribution on each spectra for  $5600 \text{ \AA}$ , with an error of order 5%.

#### 4.2.3. The Nonstellar Continuum

Once the stellar population contribution was subtracted from all spectra, we have analyzed the nonstellar or featureless continuum, originated at the central source.

TABLE 3  
RESULTS FROM THE CONTINUUM ANALYSIS

Run (1)	Scaling Factor (2)	Percent at $5600 \text{ \AA}$ (3)	Spectral Index (4)
1 .....	1.1087	41	1.5
2 .....	1	50	1.2
3 .....	1.3038	58	0.9
4 .....	1.0447	37	0.7
5 .....	1.0447	37	0.7
6 .....	1.0447	36	0.4
7 .....	1.0447	40	1.4
8 .....	0.7717	29	0.7
9 .....	1.0447	35	0.1
10 .....	1.0447	32	0.7

Our work assumption was that this component can be represented by a power law

$$F_\nu = F_0 \nu^{-\alpha} \text{ ergs cm}^{-2} \text{ s}^{-1} \text{ Hz}^{-1},$$

where  $\alpha$  (the spectral index) and  $F_0$  are positive constants, and that it would be the optical extension of the ionizing continuum, originating at the central source.

A least-squares fitting of the above function was done on a "spline" continuum traced over each spectra, for  $\lambda > 5200 \text{ \AA}$ , and the final solution was chosen as being the one that furnished the flattest spectrum and was below the observed data along all the spectral range.

The spectral indexes thus obtained are presented in Table 3. Taking into account the influence of the noise level of the spectra on the tracing of the spline continuum, an error of  $\pm 0.1$  has to be considered for these results. Figure 9 presents the spectra already free of the stellar population contribution, and the power-law continuum fitted for each epoch (hereafter referred as the PL continuum) is represented by the dashed line.

From this figure it can be seen the presence on all but two spectra (runs 2 and 9) of an excess above the PL continuum for wavelengths smaller than  $5200 \text{ \AA}$ , with variable shape, intensity, and extension. Similar features, but of smaller intensity, have been found in NGC 7469 (Bonatto & Pastoriza 1990) and Mrk 590 (Ferland, Korista, & Peterson 1990).

For run 1, the emission at  $\lambda < 3900 \text{ \AA}$  above the PL continuum can be easily attributed to the high-order Balmer lines. However, for the other spectra where it is present, the excess is much too strong and/or begins at wavelengths too large to be produced by this same mechanism. The fact that the two simultaneous spectra of 1989 May (runs 4 and 5), obtained at different observatories under different conditions (detectors, slits, standard stars), are independently fitted by the same PL continuum and present the same blue excess makes us very confident of the reality of this feature.

Our first attempt to represent this excess was with a blackbody curve, as the blue bump of AGN continua is frequently attributed to the emission by an accretion disk with  $T \approx 20,000\text{--}35,000 \text{ K}$  (Malkan 1983; Stein & O'Dell 1985; Ulrich 1989). However, the continuum shape after the subtraction of the PL continuum cannot be represented at all by a Planckian function, and a simultaneous fit of a power law plus a blackbody over the entire range of the stellar population-free spectra continuum gives the same negative result.

As the emission-line fitting procedure (see § 3) is somewhat sensitive to the continuum level, it was necessary to find an analytical representation for the excess which allowed us to suitably remove the latter from below the emission-line spectrum. The simplest mathematical function which we found to represent appropriately the excess shape is another power law  $F_\nu \propto \nu^{-\alpha}$ , but now with negative spectral indexes.

We want to stress that the above function is a representation for the observed continuum shape: it cannot be extrapolated to wavelengths below the observed spectral range on each spectrum, and we do not want to attribute this specific form to any physical mechanism (as done with the PL continuum, that can be associated with the synchrotron emission from the central source). The only physical parameter that can be obtained from the fitting of a power law to the excess is the total flux of this feature.

The fit of the excess, when present, is also shown in Figure 9 as a dash-dotted line, as well as the final representation

for the nonstellar continuum in our spectra (i.e., PL continuum + excess) as a heavy line. For the sake of homogeneity we have chosen to decompose the emission on the run 1 spectrum by these same two components instead of trying to introduce another one for the high-order Balmer lines and continuum alone. We have then subtracted these components in order to isolate the pure-line emission.

#### 4.3. The Emission-Line Analysis

The emission-line spectrum of quasars and Seyfert 1 nuclei is characterized by the presence of broad (full width at half-maximum [FWHM]  $\geq 10^3 \text{ km s}^{-1}$ ), frequently asymmetric, permitted lines which could present variability not only in flux, but also in profile (see Peterson 1988, and references therein).

To obtain a consistent representation for the emission line of our spectra (already free of all continuum contributions as described in §§ 4.2.2 and 4.2.3) we have first analyzed the variations in the line profiles, resulting from taking the difference between the various observations. This procedure is similar to the ones followed by Wamsteker et al. (1990) for NGC 5548 or Alloin, Boisson, & Pelat (1988) for Akn 120 and permits to isolate the individual variable components.

We have performed differences between all the CTIO and CASLEO spectra, that have similar resolutions, and a total of 17 differences presented variations with enough amplitude to permit an adequate decomposition in one or more Gaussian components, employing a method based on the technique described by Pelat & Alloin (1980) and used before by Bonatto & Pastoriza (1990).

The standard model (Table 4) obtained to describe the permitted lines of NGC 3783, is, then, composed of by no more than six components, defined in such a way that any other one was not necessary to fit any line in the entire set of spectra, although it was not necessary for all the components to be present on all the lines and/or all the spectra. The forbidden lines are represented by one or two Gaussians (the *N*- and *I*-components of the standard model). The doublets of the [Ne III]  $\lambda\lambda 3869, 3968$ , [O III]  $\lambda\lambda 4959, 5007$ , [O I]  $\lambda\lambda 6300, 6363$ , and [N II]  $\lambda\lambda 6548, 6584$  lines are constrained to have the theoretical ratio of intensities and separation, and the same FWHM (in  $\text{km s}^{-1}$ ). The [S II]  $\lambda\lambda 6717, 6731$  lines are constrained on theoretical separation and on equal FWHM. We first attributed only one component to each forbidden line, except the [O III]  $\lambda\lambda 4959, 5007$  lines. If the final fit is not satisfactory another component is included or the *I*-component of [O III] is suppressed. None of the fits accepts a third component for [O III].

The model constitutes the set of initial parameters furnished to the fitting routine: as a first guess, the six components are associated to each permitted line, with intensities estimated by eye, and central wavelengths and FWHM given by the model.

TABLE 4  
STANDARD MODEL

Component	Symbol	$\lambda_0$	FWHM ( $\text{\AA}$ )
Narrow .....	N	Emission	[O III] lines
Intermediate .....	I	Emission	30
Broad .....	B	Emission	70
Very broad .....	VB	Emission	150
Blue wing .....	BW	Emission $-20 \text{ \AA}$	40
Red wing .....	RW	Emission $+40 \text{ \AA}$	60

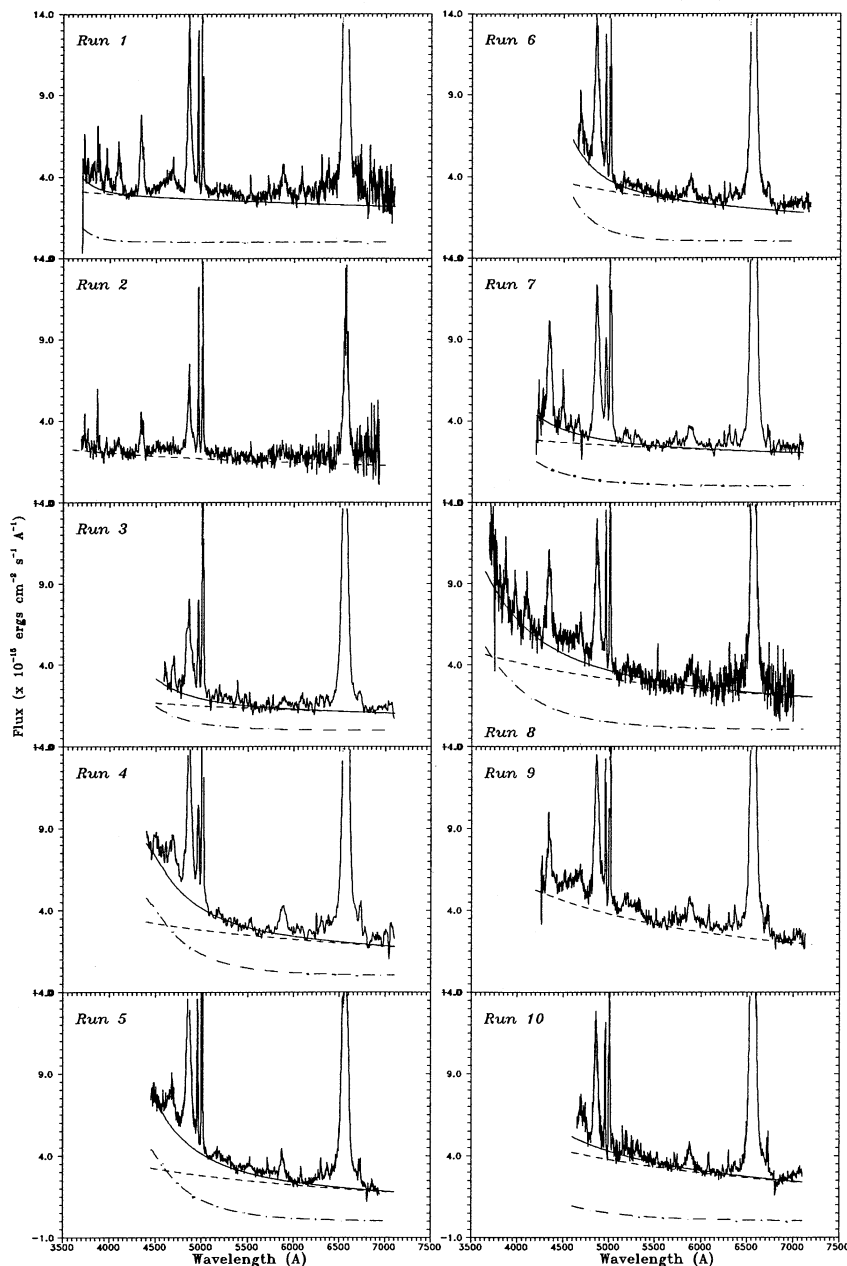


FIG. 9.—The nonstellar continuum decomposition. The stellar population-free spectra are arranged in chronological order from top to bottom and from left to right. The dashed line is the PL continuum; the dash-dotted line is the power law fitted to the excess; and the solid line is the sum of these two contributions.

Once the convergence is achieved, or concluding by the inexistence of a local minimum on the reduced  $\chi^2$  for the guess, the results are examined, and any component that has diverged on FWHM or  $\lambda_0$  away from the fitting region, or finalized with an intensity below the noise level, is excluded from the fit.

The entire procedure is repeated with the initial values of the standard model for the remaining components of the fit, until a reasonable representation has been obtained for the line profile (we have finalized with  $\chi^2 < 0.5$  for all the lines and less than 0.01 for the majority of them).

The fitting regions are the following:

$\lambda\lambda 3700\text{--}3750$	[O II] $\lambda 3727$
$\lambda\lambda 3800\text{--}3950$	[Ne III] $\lambda 3869$ , H $\delta$
$\lambda\lambda 3900\text{--}4200$	[Ne III] $\lambda 3968$ + H $\epsilon$ , H $\delta$
$\lambda\lambda 4250\text{--}4450$	H $\gamma$ + [O III] $\lambda 4363$

$\lambda\lambda 4400\text{--}5200$	He II $\lambda 4686$ , H $\beta$ , [O III] $\lambda\lambda 4959$ , 5007
$\lambda\lambda 5600\text{--}6150$	He I $\lambda 5875$ , [Fe VII] $\lambda 5721$ , $\lambda 6085$
$\lambda\lambda 6250\text{--}6800$	[O I] $\lambda\lambda 6300$ , 6363, [Fe X] $\lambda 6373$ , H $\alpha$ + [N II] $\lambda\lambda 6548$ , 6584, [S II] $\lambda\lambda 6717$ , 6731.

All the lines within each of the above intervals were fitted simultaneously. An example of the resulting fit is given in Figure 10.

If the several components of the emission lines are supposed to originate at distinct subregions inside the emission-line regions (ELRs), each of these subregions could be characterized by the velocity of turbulence of the gas ( $v_t \equiv \text{FWHM}$  of the Gaussian component/1.67) and by the shift of the central wavelength of the component with respect to the systemic velocity of the galaxy (hereafter  $\Delta\lambda$ ).

In order to isolate these subregions we have plotted the



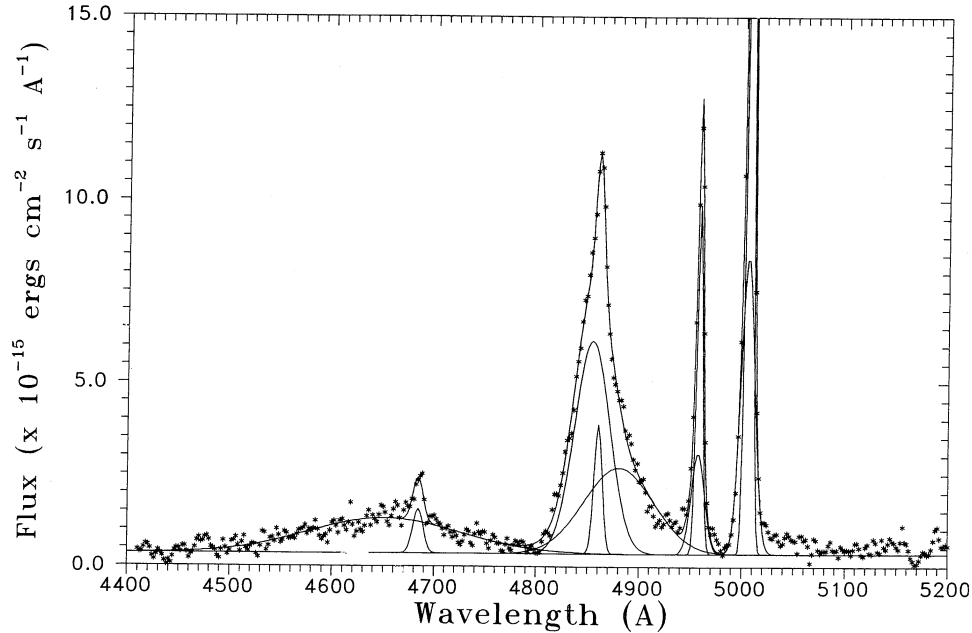


FIG. 10.—Example of the Gaussian decomposition for the He II  $\lambda 4686 + \text{H}\beta + [\text{O III}] \lambda\lambda 4959, 5007$  lines on the run 1 spectrum

FWHM of the components as a function of their  $\Delta\lambda$  for all the emission lines on each spectrum, as illustrated on Figure 11 for the run 8 spectrum. The points clearly segregate in four main regions.

When plotting the FWHM versus  $\Delta\lambda$  of the components of each permitted line, considering simultaneously all the observations, three regions are found. This result is illustrated in Figure 12a and less clearly (due to the smaller S/N of the emission lines that affects the final solution of the Gaussian decomposition) in Figures 12b and 12c.

The analysis of these figures permits us to establish the characteristics for the regions shown in Table 5.

Comparing Figures 12a and 12b, it can be noted that besides

the main regions observed both in H $\alpha$  and H $\beta$ , for the latter we have several components with turbulent velocities between 1500 and 3700 km s $^{-1}$  and wavelength shifts usually greater than 1000 km s $^{-1}$  both to the blue and red sides of the systemic velocity. These components, which we have called *transient components*, if associated with a different region (or regions), will correspond to emission by a gas with  $N_e > 10^8 \text{ cm}^{-3}$ , as they have not been detected on the forbidden line profiles.

Tables 6 and 7 present the results of the line analysis. Table 6 gives the mean narrow-line fluxes (sum of regions 1 and 2, averaged over all the observations) and Table 7, the broad-line ones (sum of regions 3, 4 and transient components, for each epoch). The values are given in units of  $10^{-15} \text{ ergs cm}^{-2} \text{ s}^{-1}$ ,

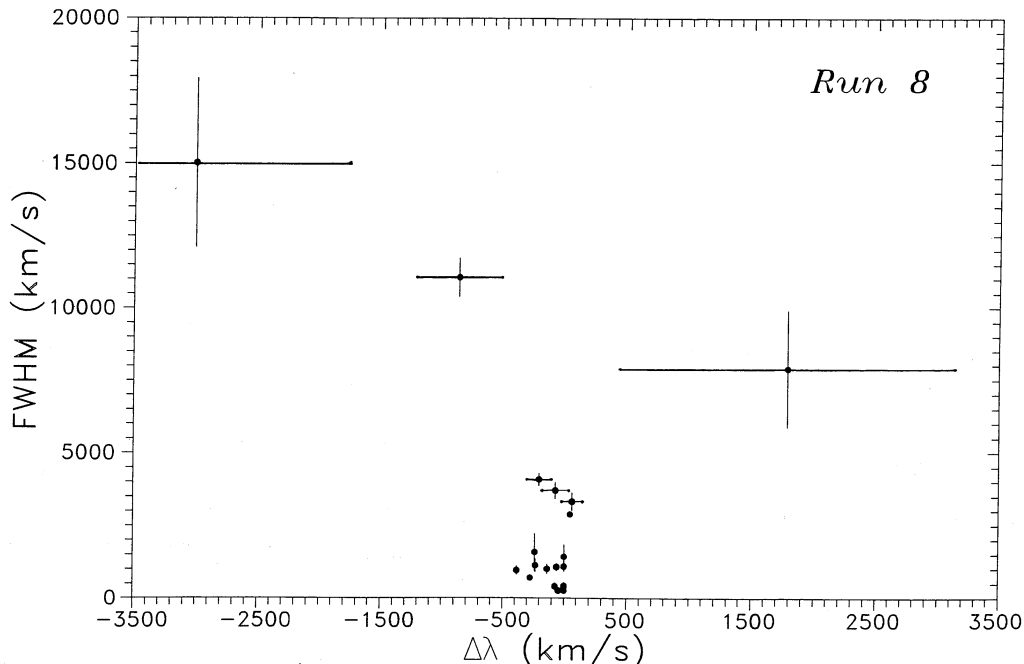


FIG. 11.—FWHM vs.  $\Delta\lambda$  plot for all lines fitted on the CTIO run 8 spectra

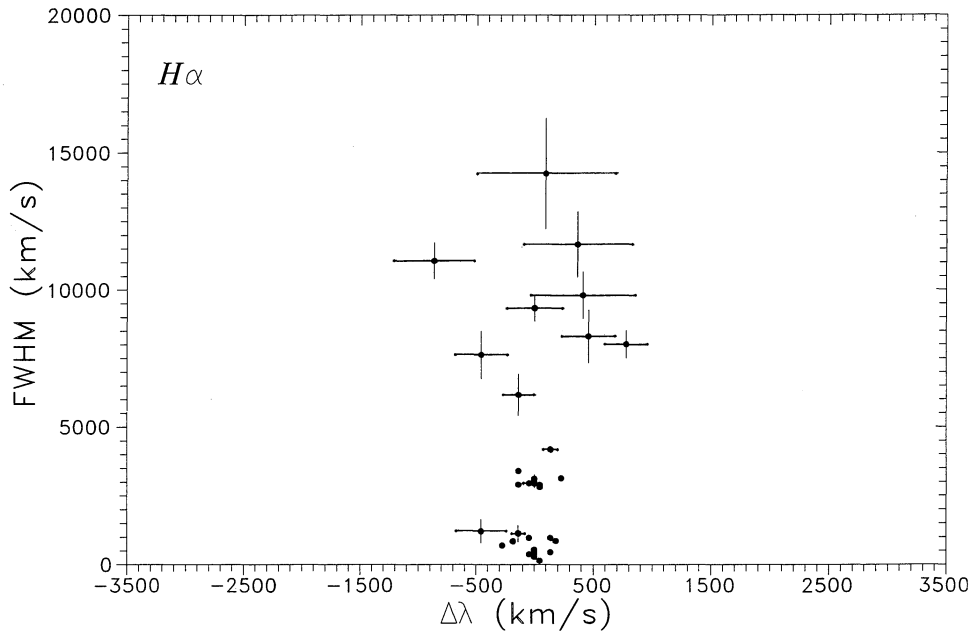


FIG. 12a

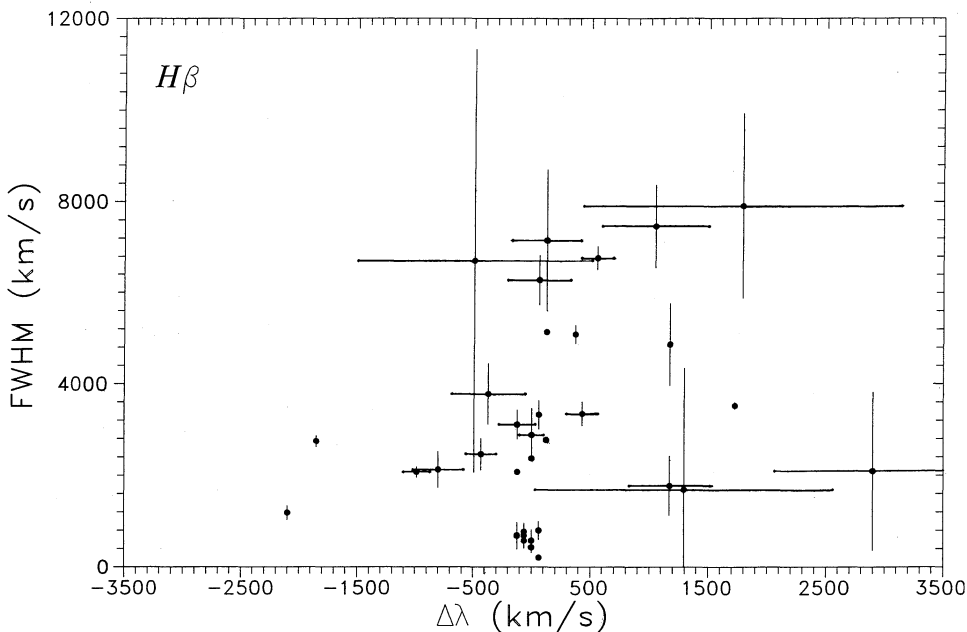


FIG. 12b

FIG. 12.—Same as Fig. 11, but for the components fitted to the permitted lines on the entire set of spectra. (a)  $H\alpha$  (b)  $H\beta$ , and (c)  $He\ II\ \lambda 4686$ .

and the errors are calculated from the standard deviation furnished by the fitting routine for each component, with a different weight given by the percentage contribution of the component to the total flux of the line.

Although the decomposition method employed here does not assure the physical reality of the emission-line subregions, the homogeneity on the parameters found for the components of the different lines corresponding to the four main regions seems to indicate that the gas responsible for their emission indeed constitutes separate systems.

#### 4.4. The NLR Physical Conditions and Abundances

In this section we will analyze the NLR contribution, characterized by regions 1 and 2 (components  $N$  and  $I$  of the standard model). Since the resolution of some spectra does not allow us to resolve these two components, we have considered in what follows the total NLR contribution represented by the sum of regions 1 and 2. This contribution will be referred to, hereafter, as the R12 emission.

First, we have verified the possibility of narrow-line variabil-

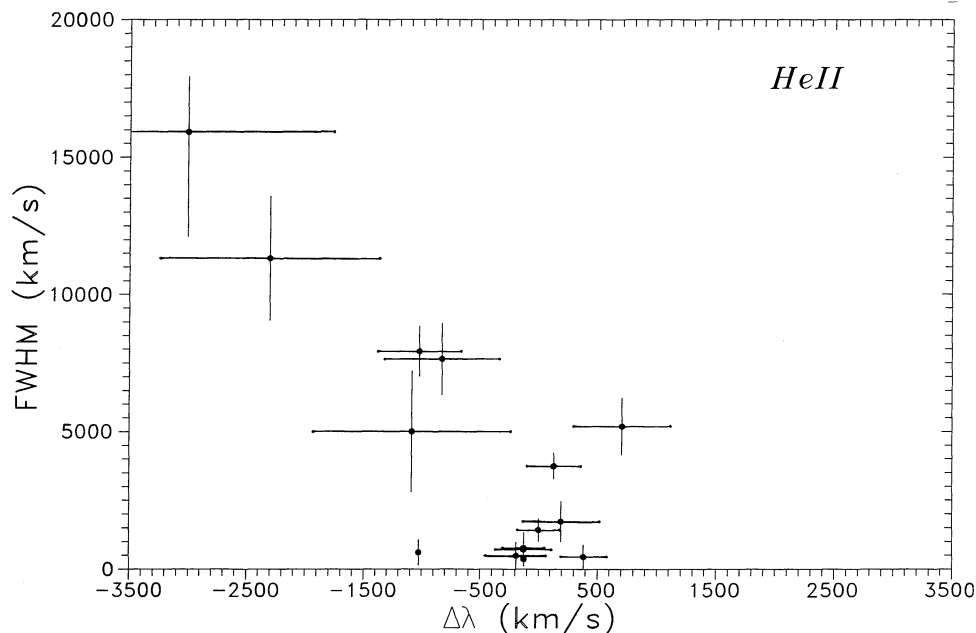


FIG. 12c

ity, and we found that the forbidden line fluxes agree within the measurement errors, even for the [Fe x]  $\lambda\lambda 6373$  line, thought to have already presented variability (Evans 1989). We have also verified that the intensities of the forbidden lines relative to that of [O III]  $\lambda 4959$  are consistent with previously published data (Evans 1988, 1989; Atwood et al. 1982). Therefore, we can extend the conclusion of Evans (1989), whose 1983 and 1984 spectra show forbidden line fluxes (relative to [O III]  $\lambda 4959$ ) consistent with previous data obtained over 10 yr from then, indicating no narrow-line variability, and assert that the time scale for emission-line variation on the NLR is at least 16 yr.

In order to calculate the physical conditions inside the R12, we have used the averaged fluxes of Table 6. From these values, we get the Balmer decrement  $H\alpha/H\beta = 3.6 \pm 1.8$ , indicating few or no internal absorption on the R12 clouds, as already discussed by Ward & Morris (1984).

The electronic temperature and density are calculated using the three-level atom approximation of McCall (1984) for the [O III]  $I(\lambda 4959 + \lambda 5007)/I(\lambda 4363)$  and [S II]  $I(\lambda 6717)/I(\lambda 6731)$  ratios. Using the [S II] ratio, we get for the density,

$$N_e = 2100^{+1300}_{-800} \text{ cm}^{-3}.$$

In the calculation of the temperature we have to consider the influence of the stratification in electronic density known to be present in the NLR of NGC 3783 (Pelat et al. 1981; Evans 1988). The critical density for collisional de-excitation for the [O III] lines is much higher than that of the [S II] lines, and the bulk of its emission comes from regions with densities near the critical value, that is, near  $10^6 \text{ cm}^{-3}$ . We have used this value (see also Storchi-Bergmann, Bica, & Pastoriza 1990) to obtain a temperature for the R12 of

$$T_e = 13200^{+1200}_{-2700} \text{ K}.$$

The ionic and He abundances are calculated using the above electronic density and temperature with the expressions of McCall (1984) for the ions, and Osterbrock (1974) for the recombination lines of  $\text{He}^+$  and  $\text{He}^{++}$ , with an adequate correction from Ferland (1986) to account for the collisional excitation of He I  $\lambda 5875$ . The results are shown in Table 8, and from them we can obtain a 2 times solar abundance of nitrogen and a one-third solar abundance of oxygen for the NLR of NGC 3783. Overabundance of nitrogen has been already found in the BLR of NGC 3783 by Koratkar (1990), and in Seyfert 2 galaxies by Storchi-Bergmann & Pastoriza (1989).

TABLE 5  
MAIN REGIONS CHARACTERISTICS

Region	$v_t$ ( $\text{km s}^{-1}$ )	$ \Delta\lambda $ ( $\text{km s}^{-1}$ )	$N_e$ ( $\text{cm}^{-3}$ )	Lines Present
1.....	$\leq 500$	$\leq 300$	$\leq 10^6$	[O I], [O II], [N II], [S II], [Ne III], Balmer lines, He I, He II, and [O III] narrow components
2.....	500–1000	$\leq 700$	$10^{6-8}$	[Fe VII], [O III], [O I], Balmer lines, He I, He II intermediate components
3.....	1800–2000	$\leq 700$	$\geq 10^8$	Balmer lines, He I broad components
4.....	$\geq 4000$	$\leq 3500$	$\geq 10^8$	Balmer lines, He I, He II very broad components

TABLE 6  
MEAN R12 FLUXES<sup>a</sup>

[O II] $\lambda$ 3727 .....	22.5 $\pm$ 5.3
[Ne III] $\lambda$ 3869, 3968 .....	45.3 $\pm$ 7.1
H $\delta$ $\lambda$ 4101 .....	10.0 $\pm$ 4.3
H $\gamma$ $\lambda$ 4340 .....	16.3 $\pm$ 6.0
[O III] $\lambda$ 4363 .....	15.1 $\pm$ 6.1
He II $\lambda$ 4686 .....	18.2 $\pm$ 9.3
H $\beta$ $\lambda$ 4861 .....	35.8 $\pm$ 10.9
[O III] $\lambda$ 4959, 5007 .....	421.4 $\pm$ 9.6
[Fe VII] $\lambda$ 5721 .....	9.0 $\pm$ 0.9
He I $\lambda$ 5875 .....	8.7 $\pm$ 7.9
[Fe VII] $\lambda$ 6085 .....	20.7 $\pm$ 3.3
[O I] $\lambda$ 6300, 6363 .....	25.9 $\pm$ 2.8
[Fe X] $\lambda$ 6373 .....	8.8 $\pm$ 5.7
H $\alpha$ $\lambda$ 6563 .....	134.4 $\pm$ 17.3
[N II] $\lambda$ 6548, 6584 .....	40.3 $\pm$ 6.1
[S II] $\lambda$ 6717 .....	11.3 $\pm$ 2.7
[S II] $\lambda$ 6731 .....	14.0 $\pm$ 1.5

<sup>a</sup> In units of  $10^{-15}$  ergs cm<sup>-2</sup> s<sup>-1</sup>.

### 5. SPECTRAL VARIABILITY

In this section we do not intend to do an accurate analysis of the spectral variability in NGC 3783, since our observations do not provide an adequate coverage of the galaxy light curve. However, some interesting characteristics of the variations can be obtained from our data.

The light curves for H $\alpha$  and H $\beta$  lines are shown on Figures 13a and 13b for the total flux of the BLR (i.e., the total flux of the line, excluded the contribution from the *N*- and *I*-components) and for the *B*- and *VB*-components separately.

It is interesting to point out the presence of two epochs where the variations in the fluxes of these lines occur in different senses: from run 5 to run 6, H $\beta$  remains constant while H $\alpha$  decreases, and from run 9 to run 10 H $\beta$  decreases while H $\alpha$  increases. When analyzed in terms of the components, this behavior is seen to be due to the H $\beta$  *VB*- and transient components, since the light curve for the *B*-component is similar for both lines.

The overall shape of the H $\alpha$  line does not vary substantially during the observations, as can be noted considering the FWHM versus  $\Delta\lambda$  plot for this line (Fig. 12a). The components are concentrated around zero wavelength shift, and the dominance of the *B*-component which responds by about 65% of the line flux, as well as the absence of transient components guarantees an almost steady line profile.

TABLE 7  
BLR FLUXES<sup>a</sup>

IDENTIFICATION	RUN									
	1	2	3	4	5	6	7	8	9	10
H $\delta$ .....	96	43	...	...	...	...	...	90	...	...
$\lambda$ 4101 .....	16	19	...	...	...	...	...	11	...	...
H $\gamma$ .....	197	62	...	...	...	...	...	175	116	...
$\lambda$ 4340 .....	31	30	...	...	...	...	...	16	15	...
He II .....	164	...	8.4	159	191	146	...	192	238	...
$\lambda$ 4686 .....	47	...	11	24	51	39	...	51	76	...
H $\beta$ .....	409	201	296	475	465	531	445	472	546	439
$\lambda$ 4861 .....	66	44	13	26	52	50	3	63	54	100
He I .....	219	137	...	144	152	136	58	...	226	130
$\lambda$ 5875 .....	54	41	...	43	40	84	43	...	43	37
H $\alpha$ .....	1816	584	720	1867	1851	1462	1444	1422	1390	1883
$\lambda$ 6563 .....	96	11	38	47	103	34	143	20	94	48

<sup>a</sup> In units of  $10^{-15}$  ergs cm<sup>-2</sup> s<sup>-1</sup>.

TABLE 8  
NLR ABUNDANCES

Identification	Value
He/H .....	0.206 $\pm$ 0.336
12 + log (O <sup>++</sup> /H <sup>+</sup> ) .....	8.24 <sup>+0.13</sup> <sub>-0.17</sub>
12 + log (O <sup>+</sup> /H <sup>+</sup> ) .....	7.10 <sup>+0.17</sup> <sub>-0.30</sub>
12 + log (O <sup>0</sup> /H <sup>+</sup> ) .....	7.72 <sup>+0.23</sup> <sub>-0.56</sub>
12 + log (O/H) .....	8.38 <sup>+0.08</sup> <sub>-0.10</sub>
log (O <sup>+</sup> /N <sup>+</sup> ) .....	0.09 <sup>+0.17</sup> <sub>-0.28</sub>
12 + log (N/H) .....	8.29 <sup>+0.17</sup> <sub>-0.26</sub>
12 + log (S <sup>+</sup> /H <sup>+</sup> ) .....	6.07 <sup>+0.20</sup> <sub>-0.40</sub>
12 + log (Ne <sup>++</sup> /H <sup>+</sup> ) .....	7.65 <sup>+0.15</sup> <sub>-0.22</sub>

The H $\beta$  profile on the other hand, is strongly asymmetric and varies in a rapid and drastic way. These variations are mainly due to the presence of the transient components, which, together with the *VB*-component are responsible by the bulk of the flux on this line, and present a wide scatter on the FWHM versus  $\Delta\lambda$  plane (see Fig. 12b).

Finally the He II  $\lambda$ 4686 line (Fig. 12c) presents the peculiarity of not admitting a clearly separated *B*-component on the emission-line decomposition, besides having a *VB*-component shifted to the blue side of the line, while all the other permitted lines show this component centered on the systemic velocity or shifted to the red wing. The first characteristic was also detected in NGC 5548 by Wamsteker et al. (1990) and interpreted by them as an evidence of a stratification in excitation and in gas velocity in this galaxy. The second one can be attributed to the presence of the N III  $\lambda$ 4640 lines (Stirpe et al. 1988) or of the Fe II multiplets 37 and 38 ( $\lambda$ 4500–4600). The Fe II emission is historically very weak in NGC 3783 (Steiner 1981; Pelat et al. 1981; Barr et al. 1983; Evans 1988), but the stronger multiplet 42 ( $\approx$   $\lambda$ 5200) is quite evident in the spectra of runs 5–10. We can tentatively associate the surgiment of these features as a response to the strong burst that occurred in 1989 (runs 4 and 5: Winkler & van Wik 1989).

In what follows we will refer to as the “excess” the residual continuum emission found on eight of our 10 spectra, after the subtraction of the PL continuum. As can be seen in Figure 9, the temporal behavior of the total continuum for  $\lambda < 5000$  Å is strongly dependent on the behavior of the excess.

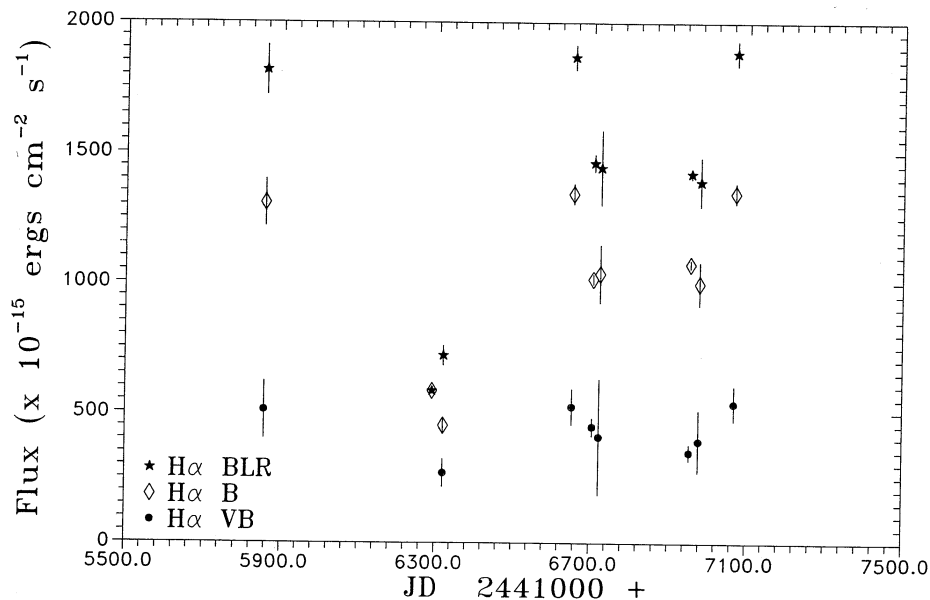


FIG. 13a

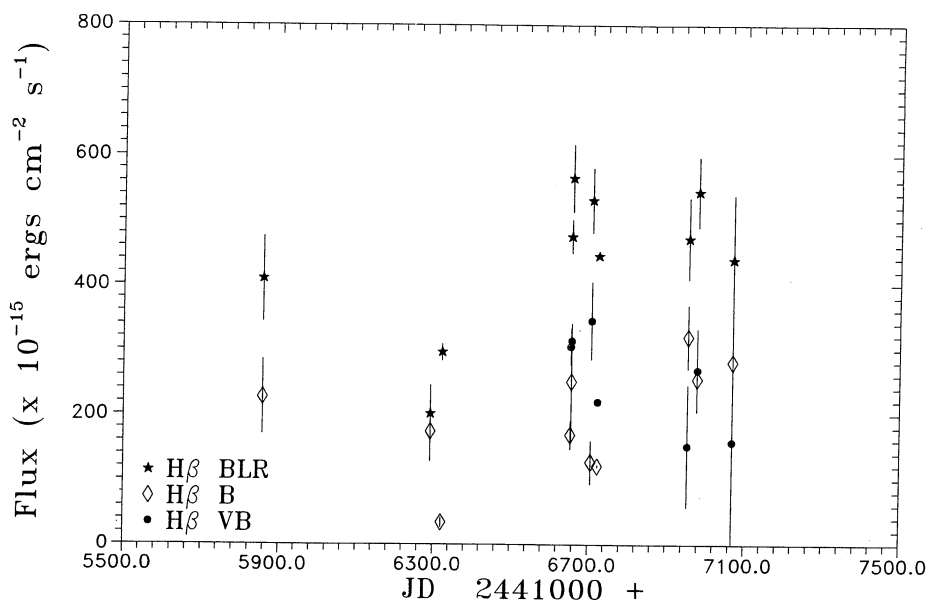


FIG. 13b

FIG. 13.—Light curve for the total BLR flux, B- and VB-components of (a), H $\alpha$ , and (b) H $\beta$ . Notice that runs 4 and 5 correspond to the same point in a.

To describe the behavior of the ionizing continuum and the overall shape of the spectra, we define: the following:  $F(5600/1450)$ : flux ratio  $F(\lambda 5600)/F(\lambda 1450)$  calculated from the PL continuum analytical form, used to represent the hardness of the ionizing continuum;  $F_{\text{EX}}$ : integrated flux of the excess, between 4650 and 7100 Å.

We now analyze the possible correlations between these two parameters and between them and the BLR fluxes. In Figure 14 is shown the dependence of the H $\beta$  BLR flux with  $F(5600/1450)$ . There is a linear correlation, in the sense that the line flux is greater when the spectrum is "harder." However, there are two points that deviate from this general behavior, corresponding to runs 1 and 7. The deviation of the run 7 point

could be tentatively attributed to a delay in the overall line response to fast falls of the ionizing continuum, such as the one which occurred between runs 6 and 7 (the power-law index turns from  $\alpha \approx 0.4$  to 1.4 in 18 days). If the behavior of the first point is also attributed to a similar delay of the emission-line gas response to continuum variations that occurred before our first observation (see Stirpe et al. 1988), and these epochs are taken as anomalous and excluded from the fit, the linear correlation between H $\beta$ (BLR) and  $F(5600/1450)$  is significant at an  $R = 0.97$  level. Similar relations, but of lower significance, are found for the BLR fluxes of H $\alpha$ , He I  $\lambda 5875$ , and He II  $\lambda 4686$  ( $R = 0.63, 0.85, \text{ and } 0.82$ , respectively), with the same two points deviating on all of them. These facts seem to indicate

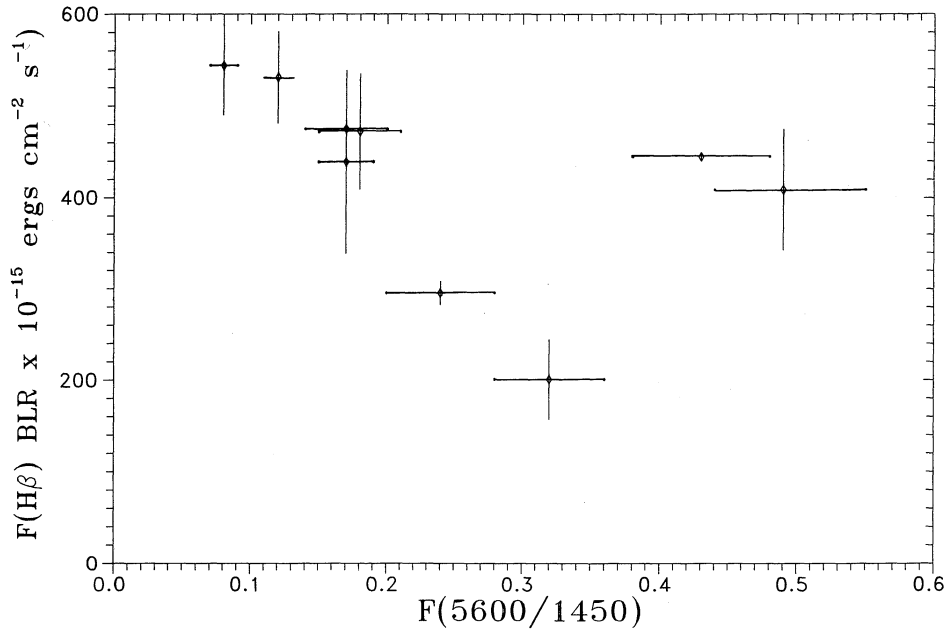


FIG. 14.—Correlation between the BLR flux of  $H\beta$  and the flux ratio of the PL continuum

that the PL continuum can be actually interpreted as the optical tail of the ionizing one. Simultaneous UV-optical observations are necessary to confirm this evidence.

On the other hand, none of the lines shows any correlation with  $F_{EX}$ . This, together with the similarity of the dependence of the integrated flux on the excess with  $F(5600/1450)$  (Fig. 15) with that of the lines, leads us to suppose that the continuum emission that constitutes the excess is generated at the BLR and driven by the ionizing continuum of the central source in a similar way to the emission lines.

Considering all the BLR emission, the Balmer decrement varies between

$$2.5 \pm 0.3 \leq H\alpha/H\beta \leq 4.7 \pm 0.3.$$

Considering the total flux of the lines, the luminosity on the period covered by our observations varied by 220% for  $H\alpha$ , 160% for  $H\beta$ , and 2300% for  $He\ II\ \lambda 4686$ , relative to the state of low activity characterized by run 2. In terms of luminosity we have

$$2.42 \times 10^{41} \leq \mathcal{L}(H\alpha) \leq 7.71 \times 10^{41} \text{ ergs s}^{-1},$$

$$8.86 \times 10^{40} \leq \mathcal{L}(H\beta) \leq 2.25 \times 10^{41} \text{ ergs s}^{-1},$$

$$3.78 \times 10^{39} \leq \mathcal{L}(He\ II) \leq 9.09 \times 10^{40} \text{ ergs s}^{-1}.$$

Using the variations on the luminosity of  $H\beta$ , we calculated the variation on the number of ionizing photons that reaches

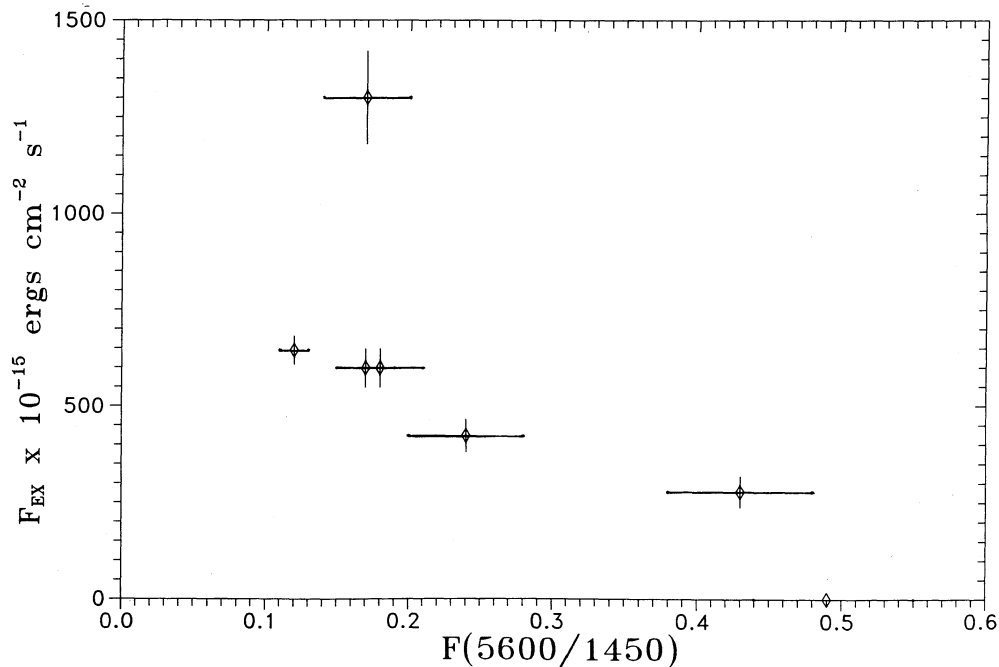


FIG. 15.—Same as Fig. 14, but now for the integrated flux on the excess

the line formation region (Osterbrock 1974):

$$3.4 \times 10^{53} \leq Q(\text{H}) \leq 8.9 \times 10^{53}.$$

With this result and typical values for the ionization parameter  $U_{\text{H}} = 10^{-2}$ , and the electronic density  $N_e = 10^9$  (Davidson & Netzer 1979), we can estimate the BLR radius as  $R \approx 0.1\text{--}0.15$  pc, which is consistent with the value obtained by Barr et al. (1983) ( $R \approx 0.1$  pc).

## 6. CONCLUSIONS

We found that the high-excitation gas in NGC 3783 is concentrated in the central  $5 \times 5$  arcsec<sup>2</sup>, while the low-excitation gas is more extended. Both distributions shows a clear asymmetry being elongated in a direction perpendicular to the bar of the galaxy. The gas in the central regions is ionized by the central source continuum, but the H $\alpha$  emission in the ring is ionized by hot stars. We have also observed the absence of gas emission along the bar of the galaxy, and from the continuum images we concluded that the light of this feature comes mainly from old stars.

Strong variations on the continuum and emission-line shape and intensity are evident in our data. We determined the bulge stellar population contribution to the nuclear light in our spectra, and we found that this contribution amounts to  $50\% \pm 5\%$  of the nuclear light at 5600 Å on a “low state” spectrum, integrated over the inner  $5 \times 5$  arcsec<sup>2</sup>.

Besides the stellar population, we represented the optical continuum by two more components: a power law with a variable positive spectral index, plus an “excess,” from  $\lambda < 5200$  Å, that cannot be represented by a blackbody curve. A multiple Gaussian component model was found to represent the emission lines on the spectra and permitted us to isolate four main emission regions, of distinct physical characteristics, plus several “transient” components, responsible for the majority of the line-profile asymmetries.

From the results of the decomposition, we separate the flux of the emission lines in the contributions from the narrow and

broad emission-line regions. The physical conditions and abundances in the NLR were calculated, and we found a Balmer decrement of  $\text{H}\alpha/\text{H}\beta = 3.6$ , a 2 times solar abundance of nitrogen and a third solar abundance of oxygen.

The analysis of the variability of the continuum and BLR line fluxes, as well as of the H $\alpha$  and H $\beta$  profiles, reveals the presence of epochs when the H $\alpha$  and H $\beta$  fluxes varied on opposite senses, due mainly to the distinct behavior of the very broad component of these lines. The line profiles are also quite distinct, with the H $\alpha$  one remaining basically the same on all the observations, while the H $\beta$  one varies drastically. We have also detected the presence of the Fe II multiplets, possibly as a response to the strong continuum burst experienced by NGC 3783 during 1989.

There is a relation between the BLR emission-line fluxes and the “hardness” of the power-law continuum, but there is no relation between the lines with the excess found above this power law. On the other hand, this excess shows a similar relation with the power-law continuum as presented by the emission lines. We can, thus, conclude that the power-law continuum is actually the optical tail of the ionizing continuum, and that the excess is generated at the emission-line region rather than at the central source.

Finally, we obtained the total variation on the luminosity of the principal permitted lines and calculated a rough estimate for the BLR radius, obtaining  $R \approx 0.12$  pc.

Our results evidence the necessity of regular and homogeneous observations of an optical-UV monitoring campaign in order to determine the full extension and the origin of the blue excess, as well as the temporal behavior and correlations of the overall continuum and emission lines.

We are grateful to H. Dottori, J. F. Santos, Jr., and R. D. D. da Costa, who kindly obtained the LNA 1989 spectra, and to E. Bica for the stellar population template. This work was partially supported by the Brazilian institutions CNPq, FINEP, and FAPERGS.

## REFERENCES

- Alloin, D., et al. 1986, *ApJ*, 308, 23  
 Alloin, D., Boison, C., & Pelat, D. 1988, *A&A*, 200, 17  
 Atwood, B., Baldwin, J. A., & Carswell, R. F. 1982, *ApJ*, 257, 559  
 Barr, P., Willis, A. J., & Wilson, R. 1983, *MNRAS*, 202, 453  
 Begelman, M. C. 1988, in *IAU Symp. 134, Active Galactic Nuclei*, ed. D. E. Osterbrock, & J. S. Miller (Dordrecht: Kluwer), 141  
 Bica, E. 1988, *A&A*, 195, 76  
 Bonatto, Ch., & Pastoriza, M. G. 1990, *ApJ*, 353, 445  
 Branduardi-Raymont, G., et al. 1985, *Adv. Space Res.*, 5, 129  
 Cooke, B. A., et al. 1976, *MNRAS*, 177, 121P  
 Davidson, K., & Netzer, H. 1979, *Rev. Mod. Phys.*, 51, 715  
 de Ruiter, H. L., & Lub, J. 1986, *A&AS*, 63, 59  
 Evans, I. N. 1988, *ApJS*, 67, 373  
 ———. 1989, *ApJ*, 338, 128  
 Ferland, G. J. 1986, *ApJ*, 310, L67  
 Ferland, G. J., Korista, K. T., & Peterson, B. M. 1990, *ApJ*, 363, L21  
 Forte, J. C., et al. 1987, *AJ*, 93, 301 (F87)  
 Glass, I. S. 1979, *MNRAS*, 186, 29P  
 Glass, I. S., et al. 1982, *A&A*, 107, 276  
 Hamuy, M., & Maza, J. 1987, *A&AS*, 68, 383  
 Koratkar, A. 1990, Ph.D. thesis, Univ. of Michigan  
 Malkan, M. A. 1983, *ApJ*, 268, 582  
 Martin, W. L. 1974, *MNRAS*, 168, 109  
 McCall, M. L. 1984, *MNRAS*, 208, 253  
 Menzies, J. W., & Feast, M. W. 1983, *MNRAS*, 203, 1P  
 Morris, S., & Ward, S. 1988, *MNRAS*, 230, 639  
 Oke, J. B., & Gunn, J. E. 1983, *ApJ*, 266, 713  
 Osmer, P., Smith, M., & Weedman, D. W. 1974, *ApJ*, 189, 187  
 Osterbrock, D. E. 1974, *Astrophysics of Gaseous Nebulae* (San Francisco: W. H. Freeman)  
 Pelat, D., & Alloin, D. 1980, *A&A*, 81, 172  
 Pelat, D., Alloin, D., & Fosbury, R. A. E. 1981, *MNRAS*, 195, 787  
 Penfold, J. E. 1979, *MNRAS*, 186, 297  
 Penston, M. V., et al. 1977, *MNRAS*, 180, 19  
 Peterson, B. M. 1988, *PASP*, 100, 18  
 Peterson, B. M., et al. 1991, *ApJ*, 368, 119  
 Seaton, M. J. 1979, *MNRAS*, 187, 75P  
 Stein, W. A., & O'Dell, S. L. 1985, in *Astrophysics of Active Galaxies and Quasi-Stellar Objects*, ed. J. S. Miller (Mill Valley: University Science Books)  
 Steiner, J. E. 1981, *ApJ*, 250, 469  
 Stirpe, G. M., de Bruyn, A. G., & van Groningen, E. 1988, *A&A*, 200, 9  
 Stone, R. P. S., & Baldwin, J. A. 1983, *MNRAS*, 204, 347  
 Storchi-Bergmann, T., Bica, E., & Pastoriza, M. G. 1990, *MNRAS*, 245, 749  
 Storchi-Bergmann, T., & Pastoriza, M. G. 1989, *ApJ*, 347, 195  
 Taylor, B. J. 1984, *ApJS*, 54, 259  
 Ulrich, M.-H. 1989, in *Theory of Accretion Disks*, ed. F. Meyer, et al. (Dordrecht: Kluwer), 3  
 Wamsteker, W., & Barr, P. 1985, *ApJ*, 292, L45  
 Wamsteker, W., et al. 1990, *ApJ*, 354, 446  
 Ward, M., & Morris, S. 1984, *MNRAS*, 207, 867  
 Ward, M., et al. 1987, *ApJ*, 315, 74  
 Winge, C., Storchi-Bergmann, T., & Pastoriza, M. G. 1990, in *ESO/CTIO Workshop Bulges of Galaxies*, ed. B. Jarvis & D. Terndrup (Garching: ESO), 325  
 Winkler, H., & van Wilk, F. 1989, *IAU Circ.*, No. 4765